Article

Effect of Niobium Addition on the High-Temperature Oxidation Behavior of 22Cr25NiWCoCu Stainless Steel in Air

Sheng-Yao Huang [1], Wen-Ta Tsai [1], Yeong-Tsuen Pan [2], Jui-Chao Kuo [1,*], Hsien-Wei Chen [3] and Dong-Yih Lin [4]

[1] Department of Materials Science and Engineering, National Cheng-Kung University, Tainan 701, Taiwan
[2] New Materials Research & Development Department, China Steel Corporation, Kaohsiung City 812, Taiwan
[3] Department of Materials Science and Engineering, City University of Hong Kong, 4/F Fong Yun Wah Building, Tat Chee Avenue, Kowloon 999077, Hong Kong, China
[4] Department of Chemical and Materials Engineering, National University of Kaohsiung, Kaohsiung City 811, Taiwan
* Correspondence: jckuo@mail.ncku.edu.tw; Tel.: +886-6-2757575 (ext. 62939)

![check for updates]

Abstract: The oxidation behavior of 22Cr25NiWCoCu stainless steel with 0–0.86 wt.% Nb addition was investigated at 900 °C in air. With an increase in Nb addition, the volume fraction and average particle size of Nb (C, N) increased, but the grain size decreased. The results of grazing incidence X-ray diffraction indicated that the steels with Nb additions promoted Cr_2O_3 formation. After 10–100 h of oxidation, Cr depletion occurred at the region with Nb (C, N) precipitates because of its high Cr consumption rate, leading to Fe oxide generation. Finally, after 100 h of oxidation, the outer layer of Fe_2O_3 and the inner layer of $(Cr, Fe, Mn)_3O_4$ were formed.

1. Introduction

According to a global energy report from the International Energy Agency, the amount of CO_2 emissions increased from 23 gigatons (Gt) to 32.5 Gt from 2000 to 2017 [1]. Reducing CO_2 emissions is necessary to decrease their impact on the environment. CO_2 emission is generally reduced in two ways: one is to improve thermal efficiency, and the other is to capture CO_2 from the end-of-pipe fuel gas [2]. Given that thermal efficiency can be improved by increasing the working temperature, the materials applied as parts of power generators may face harsh working conditions such as high temperatures (700–760 °C) and high steam pressures (30–35 MPa). Accordingly, the materials must have good high-temperature mechanical properties and oxidation resistance. In general, the best candidate materials are Ni-based superalloys (for example, Inconel and Incoloy alloys) because of their superior mechanical properties (tensile stress and creep resistance) and corrosion resistance (hot corrosion and high-temperature oxidation); however, their costs are also relatively high. Thus, austenitic stainless steels with high chromium (Cr, 16–30 wt.%) and nickel (Ni, > 20%) content should be the focus in the development of high-temperature applicable materials.

Alloys with high Cr content, such as AISI 310SS and 20Cr-25Ni-Nb stabilized stainless steel, were chosen to improve the high oxidation resistance because they form a protective Cr_2O_3 oxide layer [3,4]. Sanicro 25, a Nb-containing austenitic stainless steel with a high-temperature oxidation resistance, was recently developed [5]. Thereafter, the oxidation behaviors of Sanicro 25 have been reported [6–10]. In studies by Intiso et al. [6,7], a thin protective oxide layer was observed in a dry environment (N_2–5% O_2) between 600–750 °C for 168 h and in a wet environment (N_2–5% O_2–10%

H_2O) at 600 °C, but local breakaway oxidation was observed when the temperature was between 700 and 750 °C. Zurek et al. conducted oxidation experiments for Sanicro 25 in Ar–50% H_2O between 600–750 °C, and its oxidation rate was slightly faster than that of alloy 617 at 600, 650, and 700 °C because a strong protective Cr_2O_3 layer formed; otherwise, an outer oxide layer enriched with Fe and Ni was observed at 750 °C [8]. In Rutkowski et al.'s studies, Cr_2O_3 had been observed in a 600 °C gas mixture [9] and a 700 °C water vapor environment [10]. Despite the good oxidation resistance of Sanicro 25 at 600–750 °C, discussions of the effect of Nb or its precipitates on the oxidation behaviors remain scarce. In an earlier study of the oxidation of 20Cr-25Ni-Nb stabilized SS, Allen et al. revealed that Nb (C, N) transformed into coarsened carbonitride Nb_3M_3(C, N) and promoted the formation of M_2O_3 during exposure to 50 Torr CO_2 at 800 °C for 15 min; a mound (nodule) was observed where the reaction occurred [11,12]. However, no further discussion was conducted about the following oxidation behaviors affected by Nb precipitates.

In our previous study, the microstructure of 22Cr25NiWCoCu-xNb stainless steel with a modified Nb content from 0–0.86 wt.% was investigated. The results showed that the average grain size was reduced with increasing Nb content, and the volume fraction and particle size of the precipitates were also changed [13]. A reduction in grain size is beneficial in oxidation resistance because the grain boundaries act as fast diffusion paths for Cr to form a protective Cr_2O_3 layer [14–18]. Otherwise, some phenomena, such as different morphologies of the oxides, could possibly be induced by the precipitates [18–20]. These occurrences have not been mentioned in these reports, and the effects caused by the precipitates during oxidation still require further investigation.

In this work, we conducted an oxidation test for 22Cr25NiWCoCu-xNb stainless steel at 900 °C in air to accelerate the process and reduce the required time. Thermal gravimetric analysis (TGA) was employed to investigate oxidation kinetics. The specimens oxidized by atmospheric furnace were used to observe the formation of corrosion products over time. Grazing incidence X-ray diffraction (GI-XRD) was applied to identify the oxides formed on the surface, and the software TOPAS was used to calculate the fractions of Cr_2O_3, M_3O_4, and Fe_2O_3. Scanning electron microscopy (SEM) was employed to analyze the microstructures on the surface and the cross-sections of the oxide layer. Electron backscatter diffraction (EBSD) can be applied in the analysis of the oxide scale, as proven by Higginson et al. [21–23]. Kim et al. also used EBSD to examine the oxide scales of 304 stainless steels [17,24]. In the present study, EBSD was employed to analyze the orientation and phase distribution of the oxide scales, and energy-dispersive X-ray spectroscopy (EDS) was applied to help distinguish Cr_2O_3 and Fe_2O_3 in the oxide layer.

2. Experiment and Method

2.1. Materials and Sample Preparation

The chemical compositions of the steels studied are listed in Table 1. The steels were melted based on the major compositions of the commercial Sanicro 25 steel with varying amounts of Nb. The nitrogen content of the molten metal was analyzed using an oxygen and nitrogen elemental analyzer (HORIBA EMGA-920 O/N analyzer), and the other alloying elements were analyzed by an inductively coupled plasma atomic emission spectroscope ARL-4460 Metals Analyzer (Thermo Fisher Scientific, Waltham, MA, USA). The materials were produced using a vacuum induction-melting furnace. The ingot was hot rolled at 1250 °C and finished at an end-rolling temperature of 950 °C with a final reduction ratio of 85%. The hot-rolled plate was normalized at 1050 °C for 30 min to remove residual stress and annealed at 1300 °C for 2 h to ensure that the steel microstructure was homogenous.

The specimens for the oxidation experiments with dimensions of $14 \times 9 \times 1$ mm^3 were cut from the as-annealed plates, and a hole with a diameter of 1 mm was subsequently drilled at the top of the specimen for suspension. The prepared specimens were ground with SiC abrasive paper up to #1200 and ultrasonically cleaned with acetone and ethanol. The specimens were then suspended in a ceramic

crucible with a platinum wire for the oxidation tests conducted by TGA and by the atmospheric box furnace.

Table 1. Chemical composition of 22Cr25NiWCoCu stainless steels with 0–0.86 wt.% Nb.

Specimen	Fe	Cr	Ni	W	Cu	Co	N	C	Si	Mn	P	S	Nb
0-Nb	Bal.	22.20	24.40	3.39	2.90	1.47	0.23	0.07	0.19	0.49	0.009	0.005	0
0.29-Nb	Bal.	22.10	24.30	3.40	2.90	1.49	0.23	0.07	0.19	0.49	0.01	0.005	0.29
0.58-Nb	Bal.	21.90	24.20	3.36	2.90	1.45	0.23	0.07	0.20	0.49	0.01	0.005	0.58
0.86-Nb	Bal.	21.80	24.10	3.52	2.90	1.54	0.23	0.07	0.20	0.49	0.01	0.005	0.86

Remark: units in wt.%.

2.2. High-Temperature Oxidation Tests

Continuous isothermal weight changes were analyzed using TGA (NETZSCH STA 449 F3 Jupiter$^{®}$, Selb, Germany). The samples were suspended in a ceramic crucible with a platinum wire. The chamber was heated to 900 °C with a heating rate of 40 °C/min and then held for 150 h with a gas flow of 100 mL/min (laboratory air, 0.21 atm oxygen partial pressure).

Specimens for the observation of oxides were exposed to the ambient atmosphere, suspended in the ceramic crucible with a platinum wire, and directly placed into the atmospheric furnace preheated to 900 °C with exposure times of 1, 10, 25, 50, 75, 100, and 150 h. The specimens with the crucible were then removed from the furnace and air cooled at the end of the exposure. The weight change of the oxidized specimens was measured with an electronic balance (±0.01 mg).

GI-XRD (Bruker D8 Advance Series II, Bremen, Germany) was employed for the phase identification of oxidation products at 2° X-ray incidence angle. GI-XRD results were analyzed by using the software TOPAS for calculating the ratio of phases. The microstructure characterization was examined by the backscattered electron mode of the SEM (Hitachi SU-1500, Hitachi, Tokyo, Japan). The specimens for cross-sectional observation were plated with a nickel layer to avoid damaging the oxide layers during grinding and polishing. Phase distributions and crystallographic orientations of the oxide layer of the specimens oxidized for 150 h were observed using a Zeiss Supra 55 field-emission electron microscope, together with Oxford Symmetry: Symmetry CMOS Detector (Oxford instrument, High Wycombe, UK) for EBSD data collection with 20 kV accelerating voltage at 12 mm working distance under 70° tilt angle. Chemical composition characterization of the oxide layer was conducted using EDS (EDAX, Octane Elect EDS System) at 30 kV accelerating voltage and a 10 mm working distance.

3. Results and Discussion

3.1. Microstructure Analysis of As-Reannealed Specimens

Figure 1 shows the optical micrographs of the 22Cr25NiWCoCu stainless steel specimens with Nb addition. In the case of 0-Nb, no precipitate was observed, and the average grain size was 426 ± 107 μm. For 0.29-Nb addition, the average grain size decreased to 146 ± 25 μm, and the fine precipitates of Nb (C, N) were randomly distributed in the matrix. The average grain size of 0.58-Nb steel was 114 ± 12 μm, and the Nb (C, N) precipitates were fine and large sized. When the Nb addition was raised to 0.86 wt.%, the volume fraction of large-sized precipitates of Nb (C, N) increased significantly, few fine particles were observed, and the average grain size decreased to 90 ± 12 μm.

These results show that when the Nb addition increases in 22Cr25NiWCoCu stainless steels, the average grain size decreases, and the precipitates of Nb (C, N) tend to cluster. These phenomena were also observed in our previous study [13], in which the fine and coarse precipitates of Nb (C, N) simultaneously appeared. The hardness values of the four steels were ~210 HV, as shown in Table 2. These results indicated that alloyed Nb can promote the grain refinement and precipitation of Nb (C, N), but the hardness of the four steels did not exhibit substantial differences.
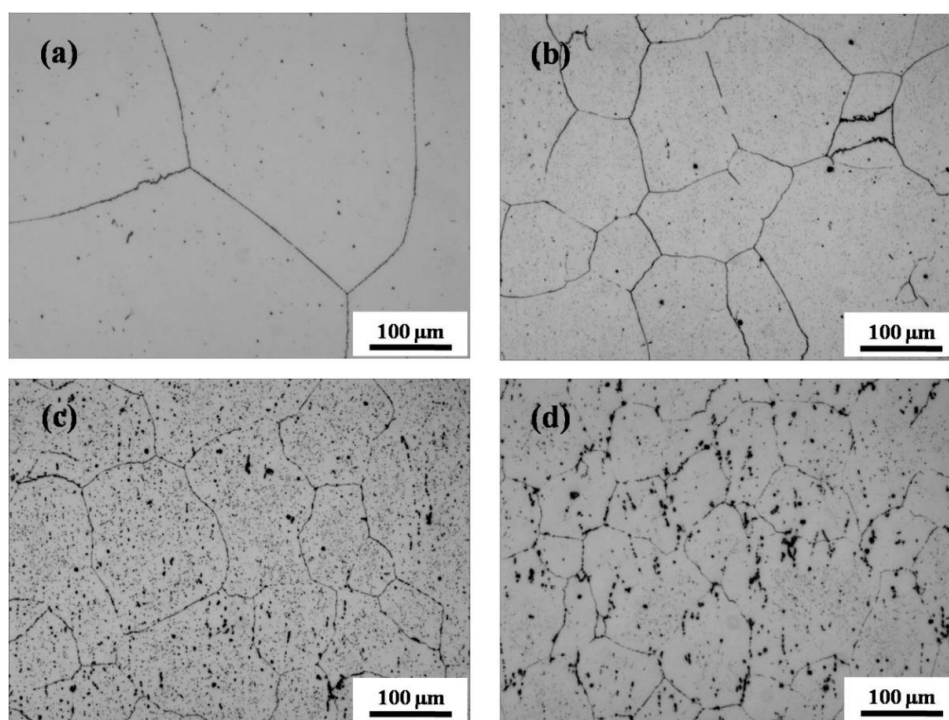
Figure 1. Optical micrograph of 22Cr25NiWCoCu stainless steels with Nb contents of (**a**) 0, (**b**) 0.29, (**c**) 0.58, and (**d**) 0.86 wt.%.

Table 2. Vickers hardness of 22Cr25NiWCoCu stainless steels with 0–0.86 wt.% Nb.

Specimen	0-Nb	0.29-Nb	0.58-Nb	0.86-Nb
Hardness (HV)	214.3 ± 8.2	218.2 ± 8.4	214.6 ± 4.6	210.9 ± 7.4

3.2. High-Temperature Oxidation Behavior

Figure 2 shows the weight gain per unit area for each specimen. Continuous measurements were conducted using TGA to investigate the change in oxides during oxidation. Discontinuous measurements were performed using an atmospheric furnace in the same oxidation conditions, and the discontinuous weight changes of individual specimens were recorded. TGA results are shown in Figure 2a, in which the solid lines represent the continuous weight changes over time, and the dotted lines are the fitting curves using the power law:

$$\Delta W = (K_P t)^{1/n} + C, \tag{1}$$

where ΔW is the weight gain per unit area; K_P, n, and C are the constants for the power law; and t is the exposure time. The fitting curves are listed in Table 3. The results show that the oxidation behaviors of 0-Nb and 0.29-Nb steels had n values of approximately 2, and those of 0.58-Nb and 0.86-Nb steels had n values larger than 3. Furthermore, 0.58-Nb steel had the highest weight gain before 46 h, but 0.86-Nb steel had the highest weight gain after 46 h, which is clearly observed in Figure 2a.

Table 3. Fitting parameters of thermal gravimetric analysis (TGA) data using the power law.

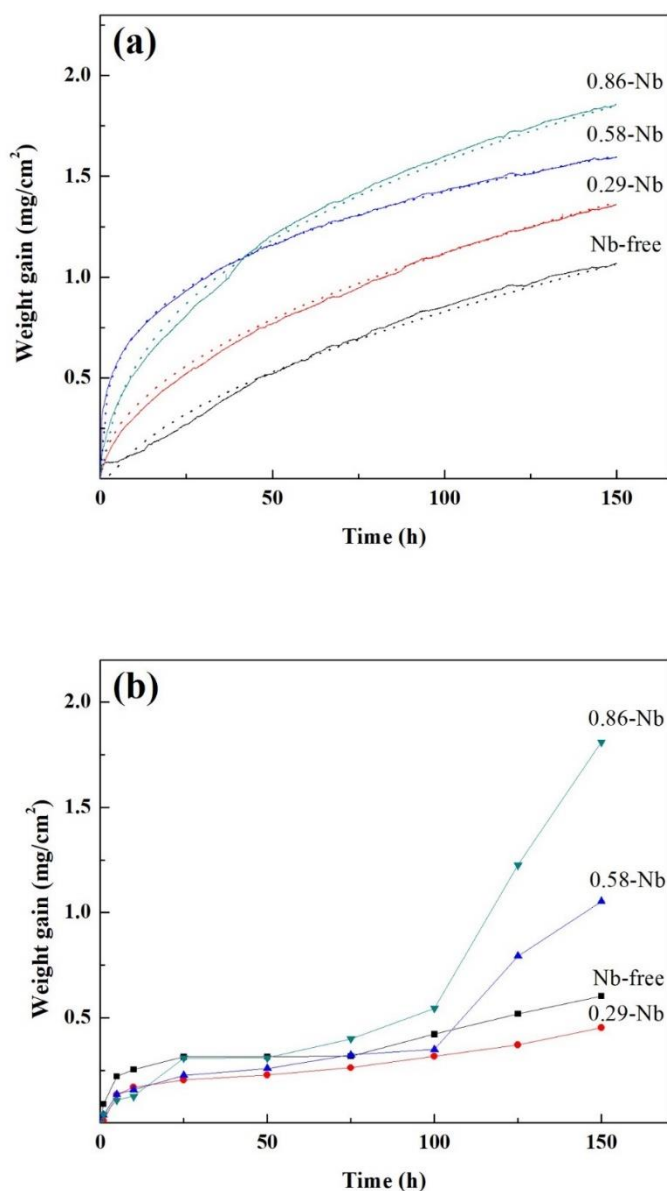| Specimen	K_{po}	n	C
0-Nb	0.08	1.86	0.54
0.29-Nb	0.10	1.92	0.52
0.58-Nb	0.44	3.70	0.27
0.86-Nb	0.44	3.08	0.32

Figure 2. Weight change per unit area as a function of time in 22Cr25NiWCoCu stainless steels with 0–0.86% Nb for continuous and discontinuous measurements in (**a**) thermal gravimetric analysis (TGA) and (**b**) an atmospheric box furnace, respectively.

Figure 2b shows the weight gain per unit area obtained from discontinuous measurements and reveals that all specimens had three oxidation stages. First, a weight gain following the parabolic growth law was observed at 10 h. A low oxidation rate was then reached. Finally, the oxidation rate increased again for 0.58-Nb and 0.86-Nb steels, where the most weight gain can be found in 0.86-Nb steel after 150 h of oxidation.

Although the test conditions for the continuous and discontinuous measurements obtained from TGA and the atmospheric furnace were similar, the weight gain curves obtained were different, as shown in Figure 2. The same specimens were employed for continuous measurements in TGA, whereas those for the atmospheric furnace were oxidized after a given time and then cooled to obtain the weight gain. The 0.58-Nb and 0.86-Nb steels showed similar measurements after long oxidation times and had higher weight gains than 0-Nb and 0.29-Nb steels. In addition, 0.86-Nb steel gained the highest weight in both tests.

3.3. Analysis of Oxide Surface Morphology

Figure 3 shows the surface morphology after 10 and 150 h of oxidation. After 10 h of oxidation, some differences were visible between the steels with and without Nb addition. In the case of 0-Nb steel, the surface morphology was homogeneous and flat, and the oxides grew along the direction of scratches, as shown in Figure 3a. Figure 3c,e,f shows that on the surface of the steels with Nb additions of 0.29, 0.58, and 0.86, some nodules were observed with average sizes of 1, 3, and 6 μm, respectively. Furthermore, the oxides formed on the nodule-free sites of Nb-added steels were homogeneous and flat, similar to those in 0-Nb steel. The surface morphology of 0-Nb steel after 150 h oxidation is shown in Figure 3b, in which the oxides remained homogeneous but with a slight increase in the oxide grain size. Figure 3d shows that the nodules of 0.29-Nb steel grew after 150 h of oxidation. Some nodules formed relatively close to the others, and the sites without nodules remained homogeneous. A significant change in the morphology of oxide was found in 0.58-Nb and 0.86-Nb steels. In Figure 3f, a porous, sponge-like oxide can be clearly seen around the nodules of the 0.58-Nb steel and is connected with the other adjacent sponge oxides. In Figure 3h, the total surface of the 0.86-Nb steel was covered with sponge-like oxide, and partial oxides started to transform into coarse oxides.
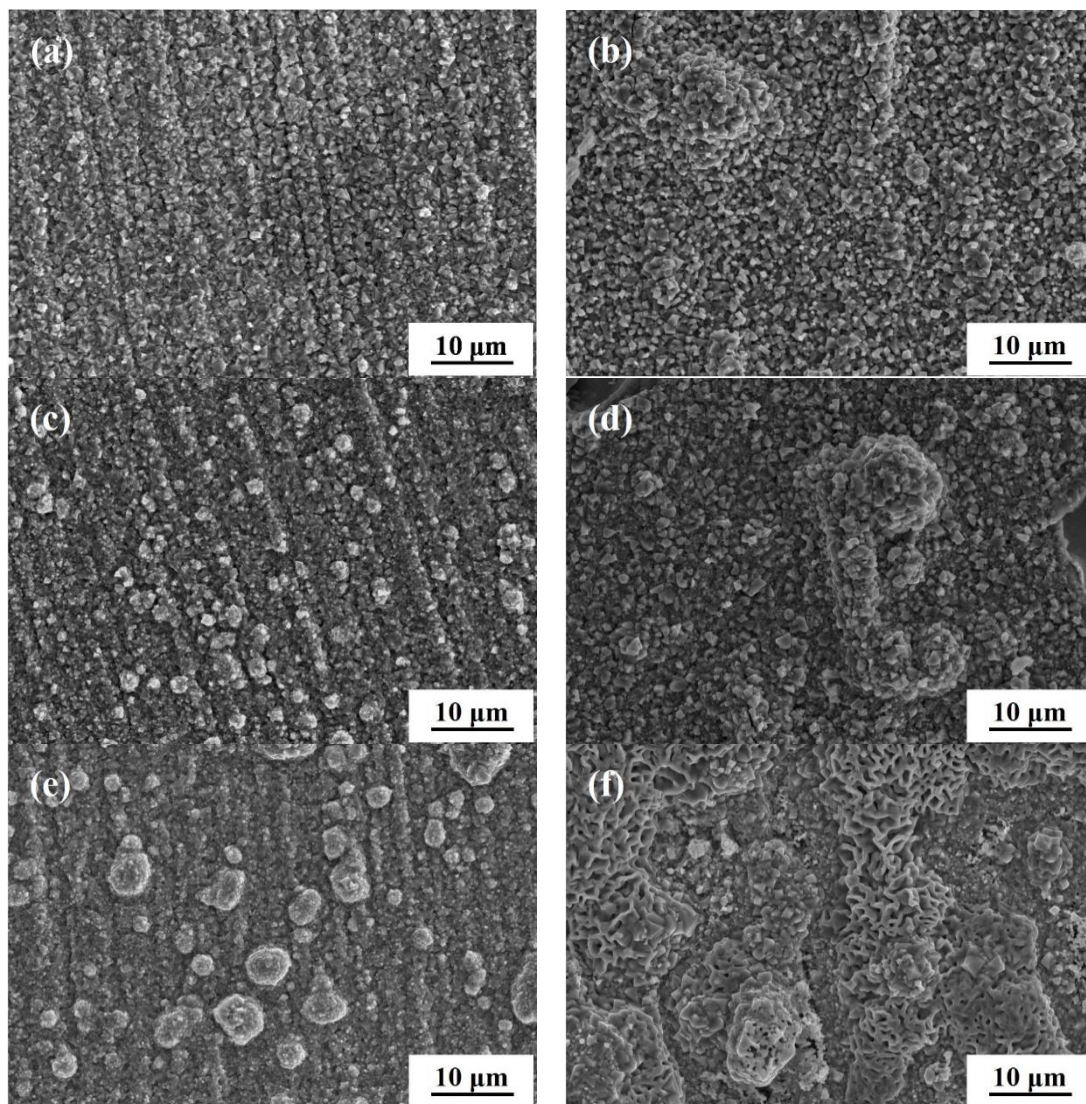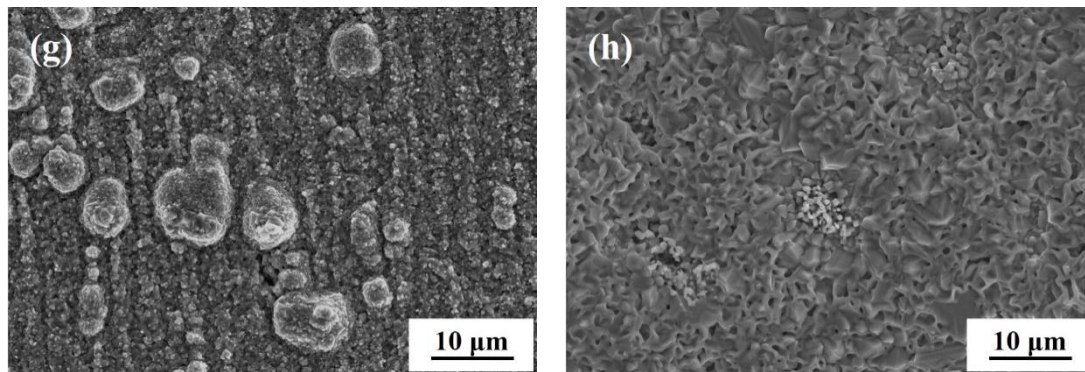

Figure 3. *Cont.*

Figure 3. SEM images of the surface morphology of 22Cr25NiWCoCu stainless steels after oxidation in ambient air (**a**) with 0% for 10 h, (**b**) with 0% for 150 h, (**c**) with 0.29% for 10 h, (**d**) with 0.29% for 150 h, (**e**) with 0.58% for 10 h, (**f**) with 0.58% for 150 h, (**g**) with 0.86% for 10 h, and (**h**) with 0.86% for 150 h.

Table 4 shows the volume fractions of Cr_2O_3, spinel $(Cr, Mn, Fe)_3O_4$, and Fe_2O_3 phases calculated using the TOPAS software. The oxides of 0-Nb steel were composed of ~65–74% Cr_2O_3 and ~21–32% M_3O_4, but Fe oxide was not detected. The oxides of 0.29-Nb steel had no Fe_2O_3, but the volume fraction of Cr_2O_3 increased to ~76–87% and that of M_3O_4 decreased to ~8–20%. The oxides of 0.58-Nb steel consisted of ~76–92% Cr_2O_3 and ~8–17% M_3O_4 within 100 h, and ~40% Fe_2O_3 was found after 150 h of oxidation. The 0.86-Nb steel was mostly composed of Cr_2O_3 (~76–93%) before 75 h of exposure, but the volume fraction of Fe_2O_3 in oxidized specimens increased from ~9 to ~53% in 100–150 h of exposure and became the major corrosion product in the outer oxide layer. GI-XRD results revealed that the volume fraction of Cr_2O_3 increased with Nb addition, and Fe_2O_3 was formed.

Table 4. Volume fractions of Cr_2O_3, M_3O_4, Fe_2O_3, and γ phases in 22Cr25NiWCoCu stainless steels with 0–0.86% Nb after oxidation in ambient air at 900 °C for an annealing time of 10–150 h obtained from grazing incidence X-ray using software TOPAS.

Specimen.	Time (h)	Cr_2O_3 (%)	M_3O_4 (%)	Fe_2O_3 (%)	γ (%)
0-Nb	10	72.1	20.6	0	7.3
	25	64.5	26.9	0	8.6
	50	66.4	32.0	0.1	1.5
	75	71.8	26.9	0.4	0.9
	100	67.8	28.0	0	4.2
	150	73.5	23.5	2.7	0.3
0.29-Nb	10	76.8	9.8	0	13.4
	25	76.0	10.1	0	13.9
	50	76.3	19.5	3.4	0.8
	75	87.4	7.5	0	5.1
	100	86.7	9.6	2.7	1.0
	150	80.5	12.3	0.9	6.3
0.58-Nb	10	75.8	8.2	0	16.0
	25	79.9	12.7	2.8	4.6
	50	82.6	17.3	0	0.1
	75	91.9	5.8	1.6	0.7
	100	90.3	6.5	2.4	0.8
	150	40.1	16.7	38.1	5.1
0.86-Nb	10	75.7	9.1	1.7	13.5
	25	86.5	11.0	2.0	0.5
	50	83.6	14.4	0	2.0
	75	93.1	6.0	0.7	0.2
	100	81.7	8.2	9.4	0.7
	150	26.5	12.1	53.1	8.3

3.4. Analysis of Oxide Layers at Cross-Section

The microstructures of the oxide layer at cross-section after 10–150 h are shown in Figure 4. A significant difference in the microstructure was found between the steels with and without Nb addition. Nodules were observed in steels with Nb addition, as shown in Figure 4b–d, but not in 0-Nb steel as shown in Figure 4a. Furthermore, oxide layers with nodules were thicker than those without nodules, and precipitates were found around the nodules. After 150 h, 0-Nb steel had a 3 µm-thick oxide layer without nodules. The formation of nodules was observed in 0.29-Nb steel, and the 10 µm-thick oxide layer of the nodule became loose. The oxide layers of 0.58-Nb and 0.86-Nb steels had thicknesses of ~12 and ~15 µm, respectively. The 0.86-Nb steel had many porous structures, whereas the 0.58-Nb steel had fewer.
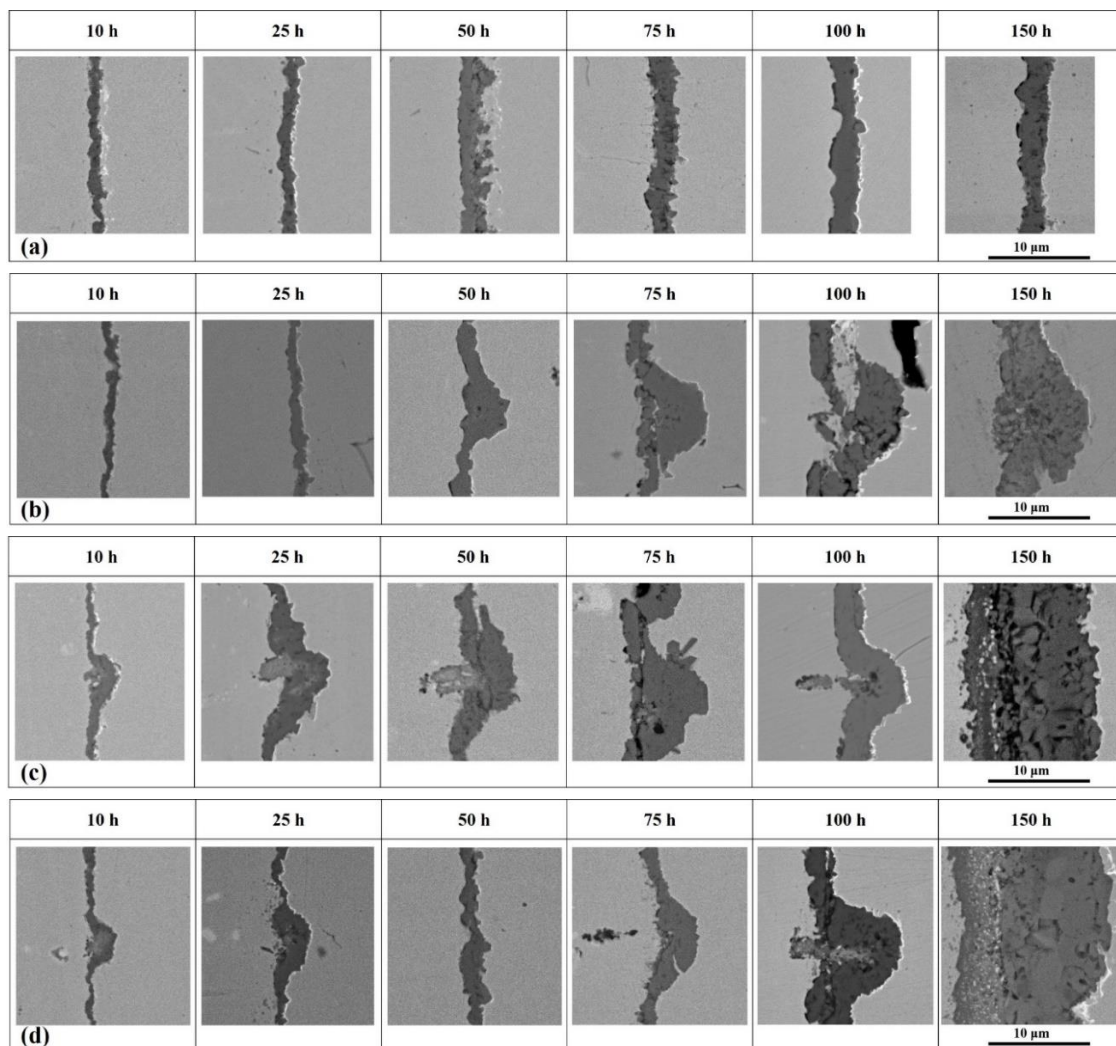

Figure 4. Optical micrograph of the oxide layer as a function of annealing time in 22Cr25NiWCoCu stainless steels with Nb contents of (**a**) 0, (**b**) 0.29, (**c**) 0.58, and (**d**) 0.86 wt.%.

Figure 5a, Figure 6a, Figure 7a, Figure 8a show the images of the oxide layers from the forward-scattered electron detector (FSD), where the white frame represents the scanning area for the EBSD analysis, and the black solid lines are the scanned regions of the EDS line scan. Figure 5b–e, Figure 6b–e, Figure 7b–e, Figure 8b–e show the results of EBSD maps and EDS line scans at the cross section of the oxide layer after 150 h, where the white dotted lines represent the interface between the oxide layer and the electroplating Ni layer. The findings of EBSD map in Figure 5e show that the major oxide layer of 0-Nb steel was composed of Cr_2O_3 and spinel $(Cr, Mn)_3O_4$. Some parts of the EBSD may

not emit a signal because of the shadow effect of the pore formation and the uneven surface at the interface. The line scan result shows that the oxide layer had Mn, Cr, and O but no Fe oxide, as shown in Figure 5f. Furthermore, the oxides of Cr_2O_3 and spinel $(Cr, Mn)_3O_4$ were columnar and did not show a preferred orientation, as displayed in Figure 5c,d.

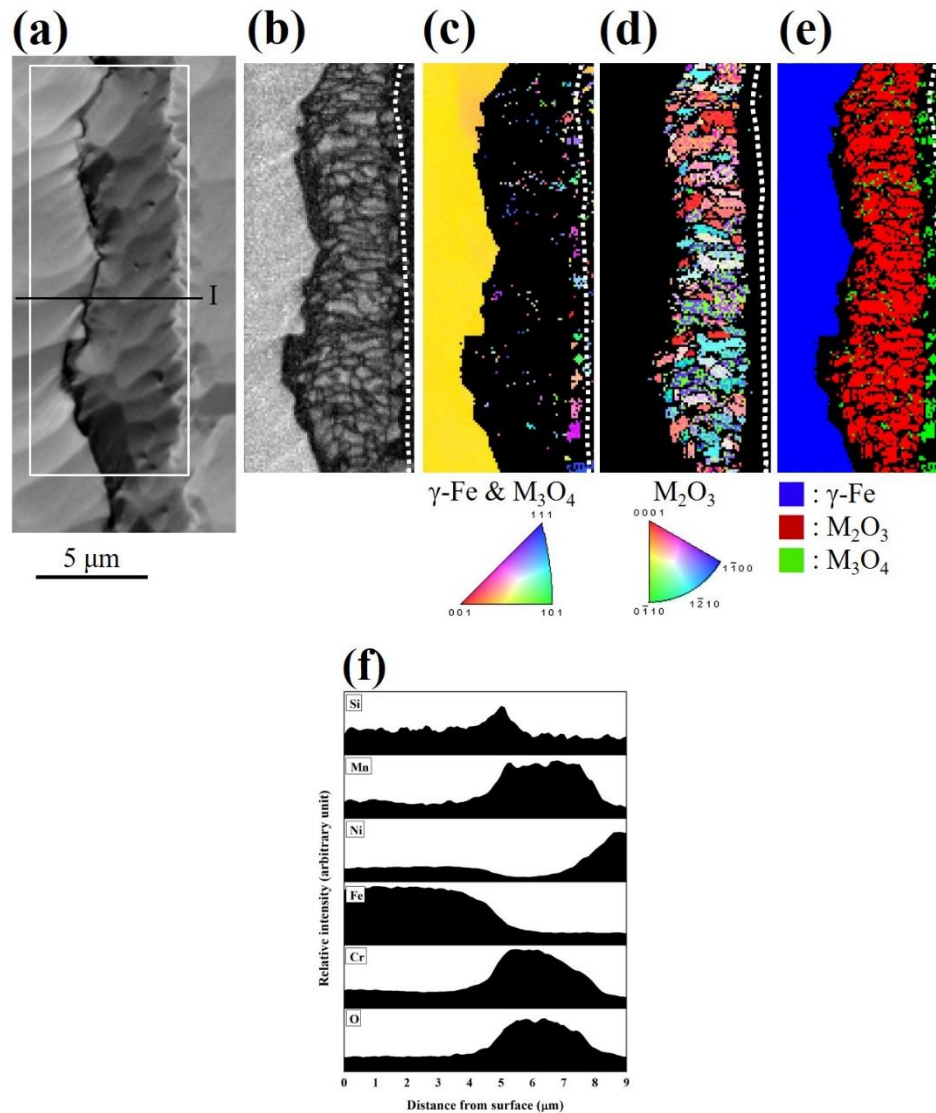**Figure 5.** (**a**) Forward-scattered electron detector (FSD) image, (**b**) image quality map, (**c**) inverse pole figure map for γ and M_3O_4 phases, (**d**) inverse pole figure map for M_2O_3 phase, and (**e**) phase map of the oxide layers in 22Cr25NiWCoCu stainless steel with 0% Nb after oxidation in ambient air for 150 h. (**f**) EDS line scan of Si, Mn, Ni, Fe, Cr, and O along line I in (**a**).

The phase map in Figure 6e and the EDS line scans in Figure 6f,g show that the major oxide of 0.29-Nb steel was Cr_2O_3, and spinel was found at the steel's outer layer. Results of EDS line scan also show an increase in Fe and a decrease in Cr at the bottom of the nodule in Figure 6f. Some of the oxide grains were almost columnar, but some were almost equiaxed where the oxides Cr_2O_3 and spinel exhibited small grain sizes and random orientations, as shown in Figure 6c,d.
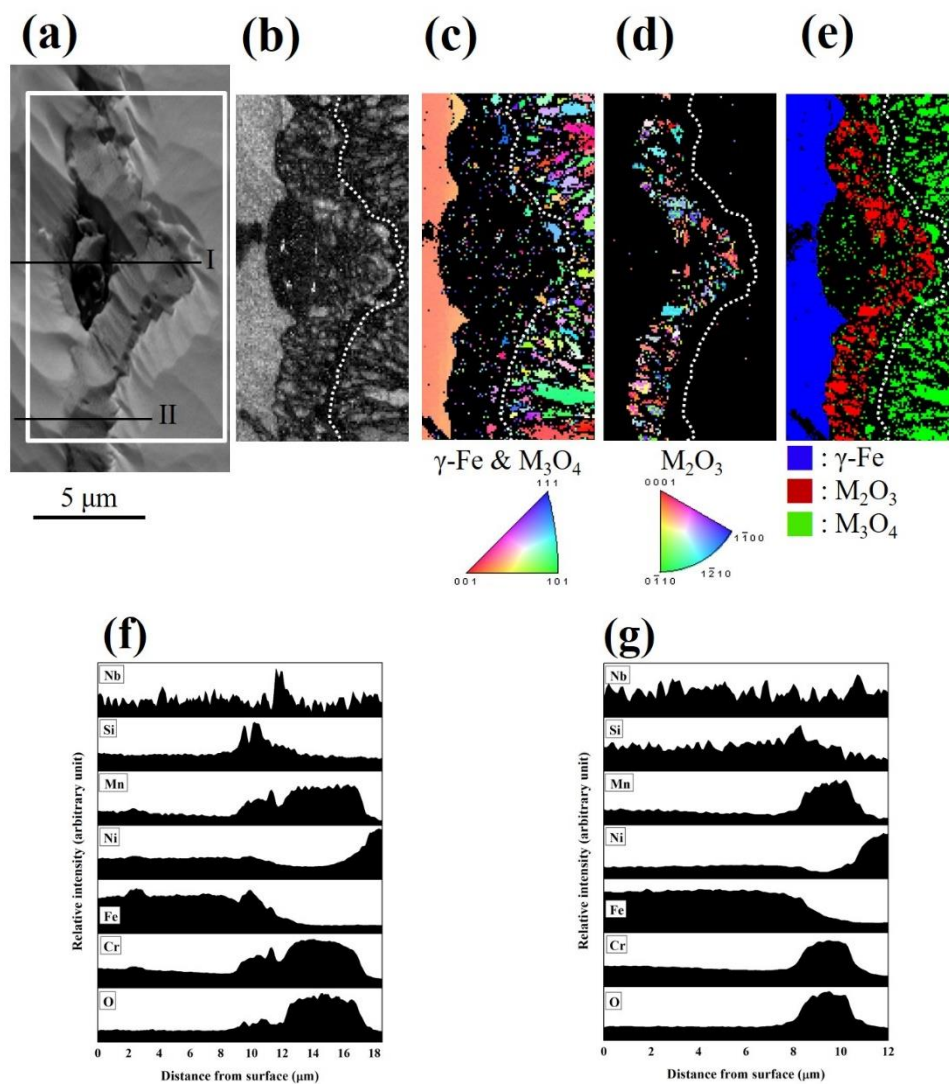
(a)   **(b)**   **(c)**   **(d)**   **(e)**

γ-Fe & M_3O_4 M_2O_3

■ : γ-Fe
■ : M_2O_3
■ : M_3O_4

(f)   **(g)**

Figure 6. (**a**) FSD image, (**b**) image quality map, (**c**) inverse pole figure map for γ and M_3O_4 phases, (**d**) inverse pole figure map for M_2O_3 phase, and (**e**) phase map of the oxide layers in 22Cr25NiWCoCu stainless steel with 0.29% Nb after oxidation in ambient air for 150 h. (**f**) EDS line scan of Si, Mn, Ni, Fe, Cr, and O along lines I and II in (**a**) and (**g**) EDS line scan of Si, Mn, Ni, Fe, Cr, and O along line II in (**a**).

In the case of 0.58-Nb steel, the phase map in Figure 7e shows that some large-sized spinel formed inside the nodules. In addition, the EDS line scan in Figure 7f shows that Fe signals were detected in the center and top surface of the nodule. A low content of Cr was also detected at the center of the nodule. These observations revealed that the high consumption of Cr led to Cr depletion around the Nb precipitates and, subsequently, led to iron oxide formation. Fine equiaxed grains of Cr_2O_3 and spinel at the oxide layer were observed, and no preferred orientation was found in the oxide grains, as shown in Figure 7c,d.
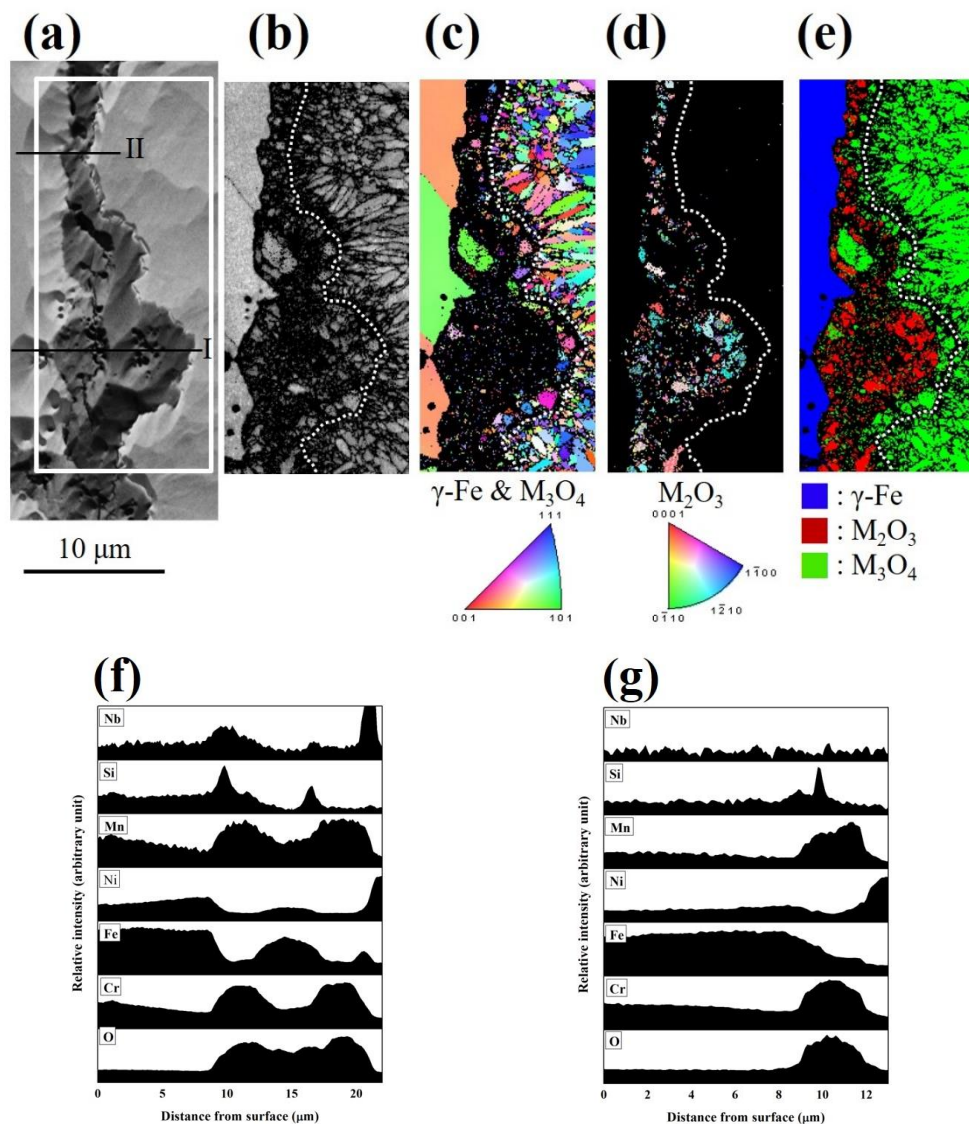
Figure 7. (**a**) FSD image, (**b**) image quality map, (**c**) inverse pole figure map for γ and M₃O₄ phases, (**d**) inverse pole figure map for M₂O₃ phase, and (**e**) phase map of the oxide layers in 22Cr25NiWCoCu stainless steel with 0.58% Nb after oxidation in ambient air for 150 h. (**f**) EDS line scan of Si, Mn, Ni, Fe, Cr, and O along lines I and II in (**a**) and (**g**) EDS line scan of Si, Mn, Ni, Fe, Cr, and O along line II in (**a**).

In 0.86-Nb steel, the major oxides in the outer layer were hematite and magnetite, the inner layer contained $(Cr, Fe, Mn)_3O_4$, and a transition layer had Cr_2O_3 between both layers, as displayed in Figure 8e–g. The oxide layer of 0.86-Nb after 150 h exposure did not have any nodules and was relatively thicker than those of the other three materials. Inverse pole figure maps show the random orientation of the oxide for the M_3O_4 and the Cr_2O_3 layers in Figure 8c,d.
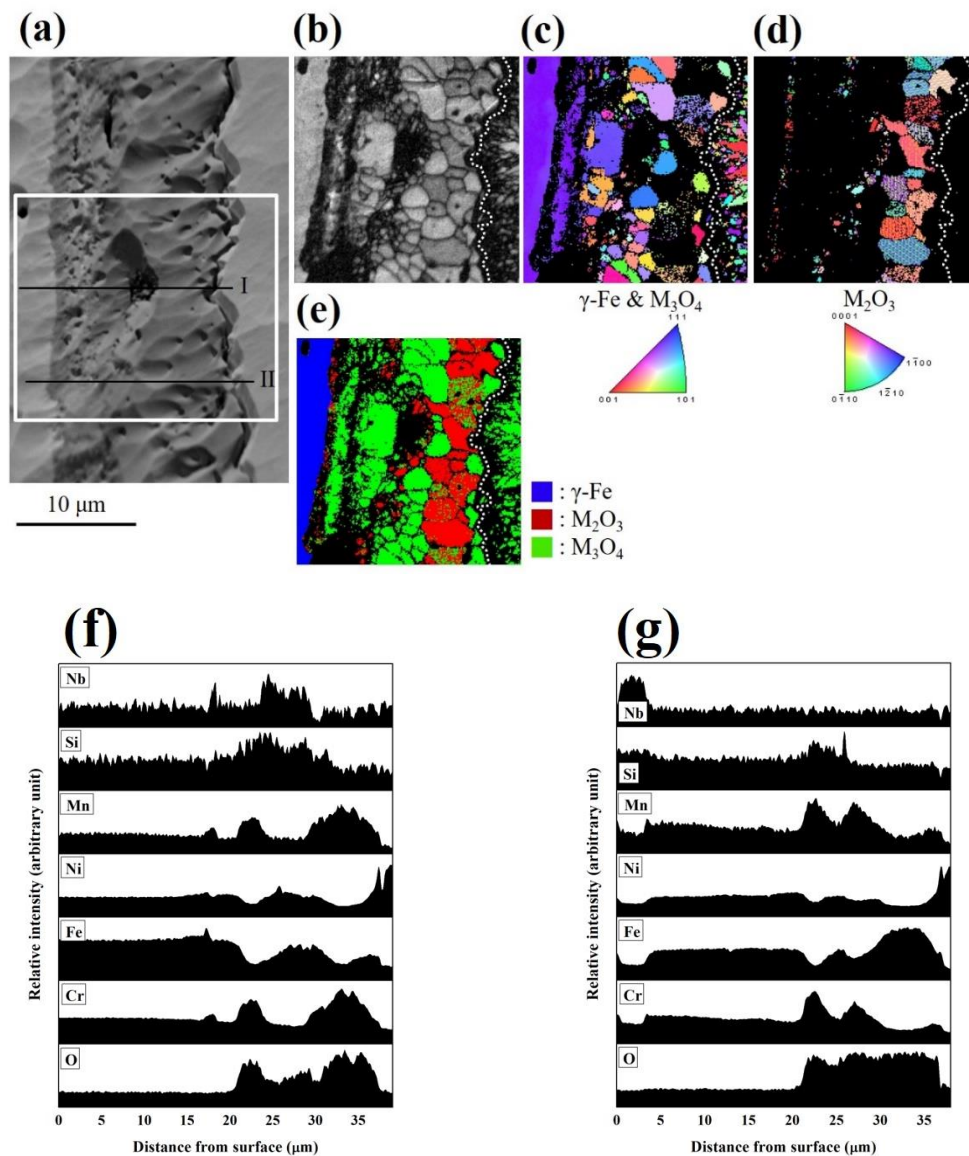
Figure 8. (**a**) FSD image, (**b**) image quality map, (**c**) inverse pole figure map for γ and M_3O_4 phases, (**d**) inverse pole figure map for M_2O_3 phase, and (**e**) phase map of the oxide layers in 22Cr25NiWCoCu stainless steel with 0.86% Nb after oxidation in ambient air for 150 h. (**f**) EDS line scan of Si, Mn, Ni, Fe, Cr, and O along lines I and II in (**a**) and (**g**) EDS line scan of Si, Mn, Ni, Fe, Cr, and O along line II in (**a**).

3.5. Effect of Nb Addition on Oxidation Behavior

An increase in Nb addition caused a decrease in the average grain size, as shown in Figure 1. According to TGA curves shown in Figure 2a, the steels with Nb additions had higher oxidation rates before 50 h than those without Nb addition. The reduction of grain size by Nb addition increased the density of the grain boundary, thus offering many outward diffusion paths for Cr and, consequently, enhancing the oxidation rate.

In 1957, Hart [25] proposed an effective volumetric diffusion that was associated with matrix and dislocation. Following Hart's concept, Smeltzer [26] proposed the effective diffusion constant as follows:

$$D_{eff} = (1 - f) * D_L + f * D_{GB}, \tag{2}$$

where D_{eff} is the effective diffusion, f is the parameter associated with grain boundaries and grain size, D_L is the lattice diffusivity, and D_{GB} is the grain boundary diffusivity. Here, f is equal to $2\delta/d$, in which

δ is the grain boundary width at approximately 0.5 nm, and d is the average grain size. Equation (2) can be rewritten as:

$$D_{eff} = D_L + f * (D_{GB} - D_L).$$ (3)

According to self-diffusion in face-centered cubic metals [27], D_{GB} is ~6 orders of magnitude higher than D_L at an oxidation temperature of 900 °C. Hence, Equation (3) can be simplified as:

$$D_{eff} = 2\delta * D_{GB}/d.$$ (4)

With the help of Equation (4), the D_{eff} for all steels is calculated as follows:

$$D_{eff}^{Nb-free} : D_{eff}^{0.29-Nb} : D_{eff}^{0.58-Nb} : D_{eff}^{0.86-Nb} = 1 : 3 : 3.8 : 4.8.$$ (5)

Apart from refining the grain size, Nb addition increased the formation of Cr_2O_3 and reduced that of M_3O_4, as shown in Table 4. Here, the formation of Cr_2O_3 and M_3O_4 lies in the inner and the outer oxide layers, as shown in Figures 5–8. Compared with the diffusion coefficients of Cr and Mn [28], that of Mn was 2 orders of magnitude higher than that of Cr. Therefore, spinel $(Cr, Mn)_3O_4$ formed at the outer oxide layer in 0-Nb steel. GI-XRD results show that the formation of Cr_2O_3 increased with Nb addition before 100 h. Cr_2O_3 was the major oxide in Nb-containing and 0-Nb steels. The reduction of grain size has a beneficial effect on the formation of Cr_2O_3 [14–19].

3.6. Effect of Precipitates on the Oxidation Behavior

According to the above-mentioned results in Section 3.5, 0.86-Nb steel should have a higher oxidation rate than 0.58-Nb steel; however, the latter obtained the highest oxidation rate. This finding indicates that the grain size did not affect the oxidation rate. According to a previous study [13], the volume fractions of Nb (C, N) precipitates for 0-Nb, 0.29-Nb, 0.58-Nb, and 0.86-Nb were 0, 3.1, 5.2, and 3.5 wt.%, respectively.

According to the microstructure of the surface (Figure 2) and cross-sectional analysis (Figures 4–8), nodules were only found in the steels with Nb addition. Small-sized nodules disappeared, and large-sized ones had grown with prolonged oxidation. Porous, sponge-like oxides initially formed at the nodules and then immediately transformed into large-sized oxides. From the cross-sectional microstructure of the oxide layer, a Nb (C, N) precipitate was always found embedded in the nodule, indicating that the formation of nodules was induced by these Nb (C, N) precipitates. These phenomena may be attributed to the high Cr consumption rate at the interface of precipitates and substrate. Therefore, the effect of precipitates contributes to the oxidation rate. This finding explains the higher oxidation rate of 0.58-Nb steel at the initial stage.

At the initial stage, a protective Cr_2O_3 layer existed on the surface, and the Cr_2O_3 oxide was the major component of oxide layer before 100 h, as shown in Table 4. Considering the effects of grain size and precipitates, 0.86-Nb steel should have the highest weight gain per unit area. After a long oxidation time, the 0.86-Nb steel had the highest weight gain per unit area. After 150 h, the Fe_2O_3 oxide became the major component of 0.58-Nb and 0.86-Nb steels. The high consumption of Cr for 0.86-Nb steel led to Cr depletion around Nb precipitates, as shown in Figure 7f. Furthermore, the Nb (C, N) at the center of the nodules led to the breakdown of the oxide layer. Thus, Cr cannot be continuously supplemented from the matrix due to Cr depletion, that is, when the concentration of Cr is lower than ~15 wt.% [14]. Fe may then start to form into a porous oxide layer of Fe_2O_3, resulting in the increased oxidation rate compared with that of the compact oxide layer of Cr_2O_3. The formation of nodules can be induced by the concentration of the protective oxide former [29–32], inhomogeneity of the chemical composition of alloy [33], surface roughness [34], breakdown of the protective oxide layer [35–37], and grain boundaries [38,39]. Allen et al. reported that the mounds (nodules) result from the phase transformation of Nb (C, N) during high-temperature oxidation [11]. In Tayler's study, Nb (C, N) was found at the center of these mounds during phase transformation [12].

According to the above discussions, a schematic diagram for the formation of the oxide layer in terms of Nb (C, N) precipitates is summarized in Figure 9 to understand the growth evolution of the oxide layer. At Stage I, a Cr_2O_3 oxide layer formed instantly on the specimen surface.
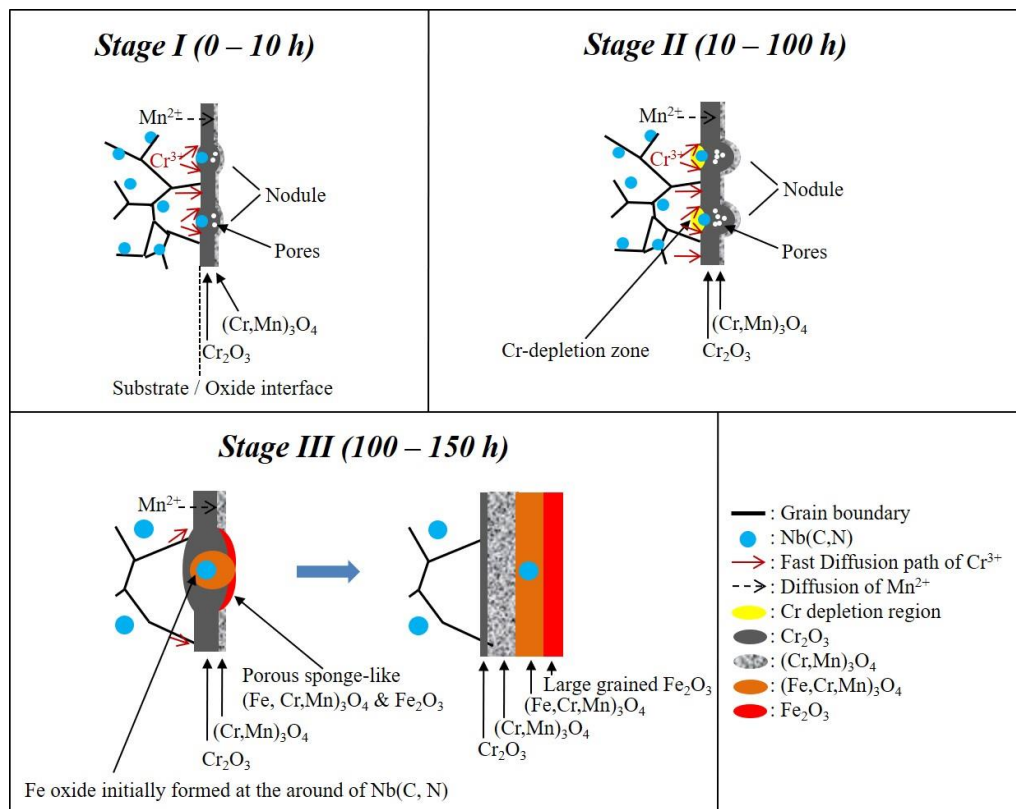

Figure 9. Schematic diagram of the growth stages of the oxide layer around Nb (C, N).

Oxide clusters were observed at the region with Nb (C, N) particles, which were imbedded in nodules. The oxide layer grew faster in the region with nodules than in the area without nodules. At Stage II, the region with nodules grew at a high Cr consumption rate, resulting in Cr depletion. Consequently, Fe oxides were initially formed at Cr-depleted zones around precipitates. Finally, at Stage III, a thick oxide layer consisting of Fe_2O_3 at the outer layer and $(Cr, Fe, Mn)_3O_4$ at the inner layer was formed.

4. Conclusions

An increase in Nb content refined the grain size from 426 to 90 μm, promoted the formation of Cr_2O_3, and avoided the formation of M_3O_4. In addition, the volume fraction of Nb (C, N) precipitates increased from 0% to 5.2% when the Nb content increased from 0–0.58 wt.%, but it decreased to 3.5% when the Nb content was 0.86 wt.%.

After 0–10 h, a Cr_2O_3 oxide layer formed, and oxide–Nb (C, N) particle clusters appeared in nodules. After 10–100 h, a high Cr consumption rate was observed in the nodule-forming regions, resulting in Cr depletion. Consequently, Fe oxides were generated at the Cr-depleted zones with Nb (C, N) precipitates. Finally, after 100 h, a thick oxide layer composed of an Fe_2O_3 outer layer and $(Cr, Fe, Mn)_3O_4$ inner layer was synthesized.

Conflicts of Interest: The authors declare no conflict of interest

References

1. International Energy Agency. Global Energy & CO2 Status Report–The latest trends in energy and emissions in 2017. Available online: https://www.iea.org/publications/freepublications/publication/GECO2017.pdf (accessed on 23 March 2018).

2. Aroonwilas, A.; Veawab, A. Integration of CO_2 capture unit using single- and blended-amines into supercritical coal-fired power plants: Implications for emission and energy management. *Int. J. Greenh. Gas. Control.* **2007**, *1*, 43–150. [CrossRef]

3. Wood, G.C.; Wright, I.G.; Hodgkiess, T.; Whittle, D.P. A Comparison of the Oxidation of Fe-Cr, Ni-Cr and Co-Cr Alloys in Oxygen and Water Vapour. *Mater. Corros.* **1970**, *21*, 900–910. [CrossRef]

4. Birks, N.; Meier, G.H.; Pettit, F.S. *Introduction to the high temperature oxidation of metals*, 2nd ed.; Cambridge University Press: Cambridge, UK, 2006; ISBN 978-0-521-48042-0.

5. Chai, G.; Nilsson, J.O.; Boström, M.; Högberg, J.; Forsberg, U. Advanced Heat Resistant Austenitic Stainless Steels. In *Advanced Steels: The recent scenario in steel science and technology*; Weng, Y., Dong, H., Gan, Y., Eds.; Springer-Verlag GmbH: Heidelberg, Germany, 2011; pp. 385–396, ISBN 978-3-319-19165-2.

6. Intiso, L.; Johansson, L.G.; Canovic, S.; Bellini, S.; Svensson, J.E.; Halvarsson, M. Oxidation Behaviour of Sanicro 25 (42Fe22Cr25NiWCuNbN) in O_2/H_2O Mixture at 600 °C. *Oxid. Met.* **2012**, *77*, 209–235. [CrossRef]

7. Intiso, L.; Johansson, L.G.; Svensson, J.E.; Halvarsson, M. Oxidation of Sanicro 25 (42Fe22Cr25NiWCuNbN) in O_2 and O_2 + H_2O Environments at 600—750 °C. *Oxid. Met.* **2015**, *83*, 367–391. [CrossRef]

8. Zurek, J.; Yang, S.M.; Lin, D.Y.; Hüttel, T.; Singheiser, L.; Quadakkers, W.J. Microstructural stability and oxidation behavior of Sanicro 25 during long-term steam exposure in the temperature range 600–750 °C. *Mater. Corros.* **2015**, *66*, 315–327. [CrossRef]

9. Rutkowski, B.; Gil, A.; Czyrska-Filemonowicz, A. Microstructure and chemical composition of the oxide scale formed on the Sanicro 25 steel tubes after fireside corrosion. *Corrosion Sci.* **2016**, *102*, 373–383. [CrossRef]

10. Rutkowski, B.; Galanis, A.S.; Gil, A.; Czyrska-Filemonowicz, A. A novel approach to the characterization of thin oxide layers. *Mater. Lett.* **2016**, *173*, 235–238. [CrossRef]

11. Allen, G.C.; Tempest, P.A.; Tyler, J.W.; Wild, R.K. Oxidation behavior of 20%Cr/25%Ni/Nb stabilized stainless steel in CO_2 environments. *Oxid. Met.* **1984**, *21*, 187–203. [CrossRef]

12. Tyler, J.W. Characterization of the initial oxide formed on annealed and unannealed 20Cr-25Ni-Nb-stabilized steel in 50 torr CO_2 at 973 K. *Oxid. Met.* **1985**, *24*, 149–176. [CrossRef]

13. Huang, S.Y.; Kuo, J.C.; Tsai, W.T.; Lin, D.Y.; Pan, Y.T. Effect of Niobium on Microstructure and Precipitation in As-annealed Sanicro 25 Steel. *Ironmak. Steelmak.* **2018**. [CrossRef]

14. Lobb, R.C.; Evans, H.E. A determination of the chromium concentration for 'healing' layer formation during the oxidation of chromium-depleted 20Cr-25Ni-Nb stainless steel. *Corrosion Sci.* **1984**, *24*, 385–396. [CrossRef]

15. Ledjeff, K.; Rahmel, A.; Schorr, M. Influence of Metal Grain Growth on the Oxidation Behavior of a 25Cr-20Ni Steel. *Oxid. Met.* **1981**, *15*, 485–493. [CrossRef]

16. Trindade, V.B.; Krupp, U.; Hanjari, B.Z.; Yang, S.; Christ, H.J. Effect of alloy grain size on the high-temperature oxidation behavior of the austenitic steel TP 347. *J. Mater. Res.* **2005**, *8*, 371–375. [CrossRef]

17. Kim, J.H.; Kim, D.I.; Suwas, S.; Fleury, E.; Yi, K.W. Grain-Size Effects on the High-Temperature Oxidation of Modified 304 Austenitic Stainless Steel. *Oxid. Met.* **2013**, *79*, 239–247. [CrossRef]

18. Peng, X.; Yan, J.; Zhou, Y.; Wang, F. Effect of grain refinement on the resistance of 304 stainless steel to breakaway oxidation in wet air. *Acta Mater.* **2005**, *53*, 5079–5088. [CrossRef]

19. Wu, Q.; Zhang, J.; Sun, Y. Oxidation behavior of TiC particle-reinforced 304 stainless steel. *Corrosion Sci.* **2010**, *52*, 1003–1010. [CrossRef]

20. Yuan, J.; Wang, W.; Zhu, S.L.; Wang, F.H. Oxidation Behavior of Super 304H Steel in Steam at 700–900 °C. *J. Chin. Soc. Corros. Prot.* **2014**, *34*, 218–224.

21. Birosca, S.; Dingley, D.; Higginson, R.L. Microstructural and microtextural characterization of oxide scale on steel using electron backscatter diffraction. *J. Microsc.* **2003**, *213*, 235–240. [CrossRef]

22. West, G.D.; Birosca, S.; Higginson, R.L. Phase determination and microstructure of oxide scales formed on steel at high temperature. *J. Microsc.* **2003**, *217*, 122–129. [CrossRef]

23. Higginson, R.L.; Jepson, M.A.E.; West, G.D. Use of EBSD to Characterise high temperature oxides formed on low alloy and stainless steels. *Mater. Sci. Technol.* **2006**, *22*, 1325–1332. [CrossRef]

24. Kim, J.H.; Kim, D.I.; Shim, J.H.; Yi, K.W. Investigation into the high temperature oxidation of Cu-bearing austenitic stainless steel using simultaneous electron backscatter diffraction-energy dispersive spectroscopy analysis. *Corrosion Sci.* **2013**, *77*, 397–402. [CrossRef]

25. Hart, E.W. On the role of dislocations in bulk diffusion. *Acta Metallurgica* **1957**, *5*, 597. [CrossRef]

26. Smeltzer, W.W.; Haering, R.R.; Kirkaldy, J.S. Oxidation of metals by short circuit and lattice diffusion of oxygen. *Acta Metallurgica* **1961**, *9*, 880–885. [CrossRef]

27. Herzig, C.; Mishin, Y. Grain Boundary Diffusion in Metals. In *Diffusion in condensed matter: Methods, materials, models*; Heitjans, P., Kärger, J., Eds.; Springer Science & Business Media: Berlin, Germany, 2006; pp. 336–366, ISBN 978-3-540-30970-3.

28. Wind, R.K. High temperature oxidation of austenitic stainless steel in low oxygen pressure. *Corrosion Sci.* **1977**, *17*, 87–104. [CrossRef]

29. Saeguas, F.; Lee, L. Oxidation of Iron-aluminum alloys in the range 500–1000 °C. *Corrosion* **1966**, *22*, 168–177. [CrossRef]

30. Tomaszewicz, P.; Wallwork, G.R. Observations of nodule growth during the oxidation of pure binary iron-aluminum alloys. *Oxid. Met.* **1983**, *19*, 165–185. [CrossRef]

31. Tomaszewicz, P.; Wallwork, G.R. The oxidation of high-purity iron-chromium-aluminum alloys at 800 °C. *Oxid. Met.* **1983**, *20*, 75–109. [CrossRef]

32. Jackson, P.R.S.; Wallwork, G.R. High temperature oxidation of iron-manganese-aluminum based alloys. *Oxid. Met.* **1984**, *21*, 135–170. [CrossRef]

33. Pint, B.A.; Wright, I.G. Long-term high temperature oxidation behavior of ODS ferritics. *J. Nucl. Mater.* **2002**, *307–311*, 763–768. [CrossRef]

34. Zhang, Z.G.; Hou, P.Y.; Gesmundo, F.; Niu, Y. Effect of surface roughness on the development of protective Al_2O_3 on Fe-10Al (at.%) alloys containing 0–10 at.% Cr. *Appl. Surf. Sci.* **2006**, *253*, 881–888. [CrossRef]

35. Wood, G.C.; Whittle, D.P. The mechanism of breakthrough of protective chromium oxide scales on Fe-Cr alloys. *Corrosion Sci.* **1967**, *7*, 771–782. [CrossRef]

36. Wood, G.C. High-Temperature Oxidation of Alloys. *Oxid. Met.* **1970**, *2*, 11–57. [CrossRef]

37. Marasco, A.L.; Young, D.J. The oxidation of Iron-Chromium-Manganese alloys at 900 °C. *Oxid. Met.* **1991**, *36*, 157–174. [CrossRef]

38. Caplan, D.; Sproule, G.I. Effect of oxide grain structure on the high-temperature oxidation of Cr. *Oxid. Met.* **1975**, *9*, 459–472. [CrossRef]

39. Atkinson, H.V. A review of the role of short-circuit diffusion in the oxidation of nickel, chromium, and nickel-chromium alloys. *Oxid. Met.* **1985**, *24*, 117–197. [CrossRef]